

## Research Article

# A Varactor-Tunable Rasorber Using Tripole and Ring Slot Elements

Qingxin Guo , Qian Chen , Jianxun Su , and Zengrui Li 

*School of Information and Communication Engineering, Communication University of China, Beijing 102004, China*

Correspondence should be addressed to Qingxin Guo; [qxguo@cuc.edu.cn](mailto:qxguo@cuc.edu.cn)

Received 13 October 2021; Revised 15 November 2021; Accepted 1 December 2021; Published 16 December 2021

Academic Editor: Shah Nawaz Burokur

Copyright © 2021 Qingxin Guo et al. This is an open access article distributed under the Creative Commons Attribution License, which permits unrestricted use, distribution, and reproduction in any medium, provided the original work is properly cited.

In this study, a frequency-selective rasorber with a tunable passband and two absorptive bands is presented. It is designed using two active FSSs, an absorptive FSS realized with tripole elements, and a lossless bandpass FSS achieved with ring slots. Both active FSSs embedded with varactors realize the shift of transmission frequency bands by controlling the bias voltage of the feed network. The working principle is briefly investigated according to an equivalent circuit model. A prototype is fabricated and measured to verify the simulated results, which show that a passband is tuned from 3 to 4.78 GHz between two absorptive bands, and the maximum band of  $|S_{11}| < -10$  dB covers from 2.2 to 7.96 GHz.

## 1. Introduction

Frequency-selective surfaces (FSSs) with both absorptive and transmissive bands have attracted much attentions in recent years because they transmit the in-band EM waves and absorb the out-of-band signals [1–3]. They are called as frequency-selective rasorber (FSR) or absorptive/transmissive frequency-selective surface (ATFSS). Some FSRs have been reported by cascading one sheet of lossy FSS which provides an absorptive feature in absorptive bands and another layer of lossless FSS which serves as a passband filter. Different structures have been utilized for designing the lossy FSS, while different slot-shape unit cells have been used for the lossless FSS [4–8]. Most of the published FSRs, including the category that realized using 3D structures [9–11], realized a fixed passband that can be lower or higher than an absorptive band or between two absorptive bands. The radomes used FSRs with fixed passband achieve not only monostatic but also bistatic radar cross-section (RCS) reduction and hence has better defense performance. But for antennas operating in different frequency bands, the radomes lack versatility. Consequently, it is necessary to actively tune the transmission bands.

Several articles presented active FSSs, among which only very few has a tunable passband [12–15], and most of them

have a switchable passband [16–20]. Some multifunctional active FSSs are also proposed by using PIN diodes in recent years [21, 22]. Figure 1 shows the concept of an FSR with two absorptive bands and one tunable passband. When an electromagnetic (EM) wave is incident onto the surface, the FSR has two different scattering properties versus the frequency of the incident wave. At the absorption bands, the signals are largely absorbed by the structure, while the useful signal between the two absorption bands can freely pass through the structure. It is a challenge to realize a tunable transmission window within two absorption bands. For a tunable or switched frequency-selective rasorber (TFSR) that is realized by using active components such as PIN diodes or varactors, the biasing network should be added into the structure. The additional network might significantly degrade the performances of the initial FSR, and the methods for insulating RF signal and DC power supply must be meticulously designed.

In this study, a TFSR with a continuous tunable passband is presented. The operating principle is illustrated with the help of its equivalent circuit model (ECM). The prototype of the proposed TFSR was tested in an anechoic chamber after being manufactured. The TFSR proposed in this study has potential application in many military systems or the protection and interference-mitigation of wireless local area network systems.

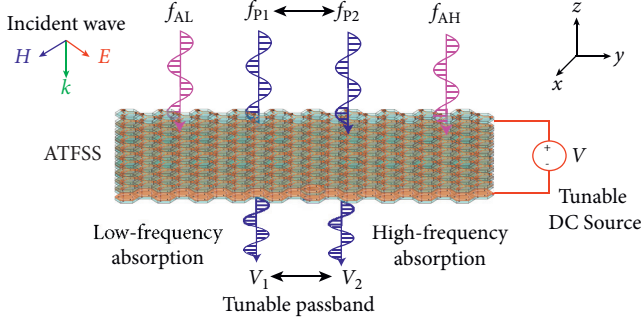


FIGURE 1: The functional diagram of the proposed FSR.

## 2. Design and Analysis of the FSR

**2.1. Structure of the TFSR.** Figure 2 shows the structure of our tunable FSR, which consists of an absorptive FSS and a bandpass FSS. The permittivity of substrate for both FSSs is  $\epsilon_r = 2.2$ , and the thickness,  $h_1 = 0.508$  mm. The space between them is denoted as  $h_2 = 12.5$  mm, which approximately equals to  $\lambda_p/4$ .

On the top layer of the absorptive FSS, three-legged loaded elements are utilized. Within each arm, a branch including two varactors  $VC_1$  and a small patch is added. To provide the necessary reverse biasing for the varactors, the three-legged loaded element on the top layer is also a part of the biasing network, and three additional narrow strips are arranged on the bottom layer of the absorptive FSS. The narrow strips are connected to the small patches on the top layer through vias. To form a return circuit for DC, the three-legged loaded elements are connected to each other by using lumped resistors ( $R_b$ ) with large resistance. In addition, six resistors are embedded in the narrow strips to mitigate the effects of the biasing network to the performance of the original FSS.

Ring slot is etched on the top layer of the bandpass FSS, as shown in Figure 2. Three varactors are placed across the slot with  $120^\circ$  angle interval. On the bottom layer, three narrow strips with three lumped resistors are applied for isolating. To mitigate the coupling between the inner and outer conducts induced by the strips, the isolating resistors are situated just beneath the slot.

**2.2. Equivalent Circuit Analysis.** Equivalent circuit is an effective method for explaining the working principle of an FSS. The basic procedures for establishing an ECM are [23–25] as follows:

- (1) The metallic strips or patches parallel to the incident  $E$  field are equivalent to inductors
- (2) The gaps between two conductors and vertical to  $E$  field, including the gaps between two elements, are equivalent to capacitors
- (3) The inductances and capacitances are obtained using the curve fitting method after the structure has been simulated with a full-wave simulator

The ECM of Figure 2 is established and shown in Figure 3, where  $Z_A$  represents the equivalent impedance of the absorptive FSS,  $Z_p$  represents the equivalent impedance of

the bandpass FSS, and the impedance  $Z_0$  and  $Z_{SUB}$  are the characteristic impedance of free space and the substrate, respectively.

The impedance  $Z_A$  consists of a series connection of  $C_1 L_1 R_1$  and a parallel connection of  $L_2 C_2 V C_1$ . The coupling between close cells is regarded as capacitance  $C_1$ . The arms mostly paralleled to the incident  $E$  field are equivalent to the inductance  $L_1$ , while the arms mainly vertical to the incident  $E$  field are equivalent to the parallel circuit of  $L_2 C_2$ . The tunable capacitor  $VC_1$  is used to tune the frequency. The capacitor  $C_{12}$  denotes the mutual coupling between two arms, which is rather small and can be ignored at low frequency. If  $C_{12}$  is ignored owing to a small value,  $Z_A$  can be expressed as follows:

$$Z_A = R_1 + j \frac{(\omega^2 L_1 C_1 - 1) [\omega^2 L_2 (C_2 + V C_1) - 1] - \omega^2 L_2 C_1}{\omega C_1 [\omega^2 L_2 (C_2 + V C_1) - 1]} \quad (1)$$

The impedance  $Z_p$  is a parallel circuit of  $L_3$ ,  $L_4$ ,  $C_3$ , and  $VC_2$ . The inductors  $L_3$  and  $L_4$  denote the equivalent capacitances of the conductor inside and outside the ring slot, and  $C_3$  is the capacitance of the slot, in which  $VC_2$  is a tunable capacitor. The impedance  $Z_p$  can be expressed as follows:

$$Z_p = -j \frac{1 - \omega^2 L_4 (C_3 + V C_2)}{\omega L_4 [1 - \omega^2 L_3 (C_3 + V C_2)]} \quad (2)$$

At the resonant frequency,

$$f_1 = \frac{1}{2\pi \sqrt{L_2 (C_2 + V C_1)}} \quad (3)$$

The imaginary part of  $Z_A$  tends to be very large; hence, only a small amount of the incoming signal from port  $P_1$  passes through  $Z_A$  and most transmit forward to port  $P_2$ . At nonresonant frequencies, part of the incident power traverses  $R_1$ , and it is inevitably absorbed by the resistor. The circuit of  $Z_p$  is parallel resonated at frequency

$$f_2 = \frac{1}{2\pi \sqrt{(L_3 + L_4) (C_3 + V C_2)}} \quad (4)$$

If  $f_1 = f_2 = f_p$ , a passband is obtained and is altered by tuning  $VC_1$  and  $VC_2$ .

The impedance  $Z_{B1}$  consisted of  $L_5$ ,  $C_4$ , and  $C_5$  and  $Z_{B2}$  consisted of  $L_6$  and  $C_6$  represent the equivalent impedance of the biasing network for the absorptive and the bandpass FSSs, respectively. Both  $Z_{B1}$  and  $Z_{B2}$  resonate at the high frequency far away from the passband because the biasing networks are divided into short strip lines by resistors  $R_b$ . They slightly affect the resonant frequencies of  $Z_A$  and  $Z_p$ , meanwhile, significantly affecting the match of the FSS at high frequency.

**2.3. Results of the TFSR.** Figures 4(a) and 4(b) show the comparison of the results of reflection and transmission coefficients got from the ECM and full-wave simulator,

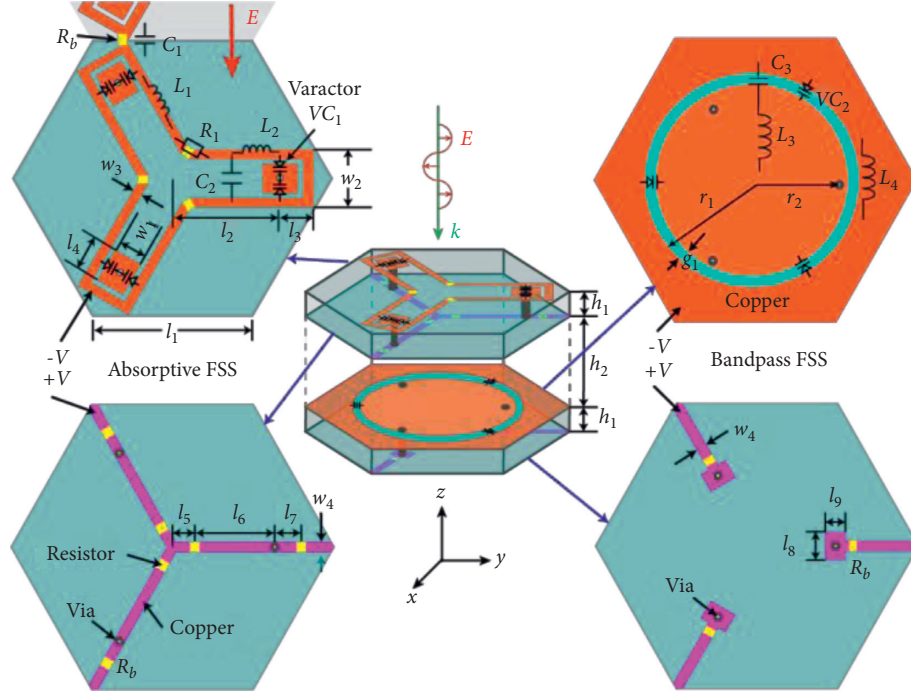


FIGURE 2: Configuration of the tunable FSR.

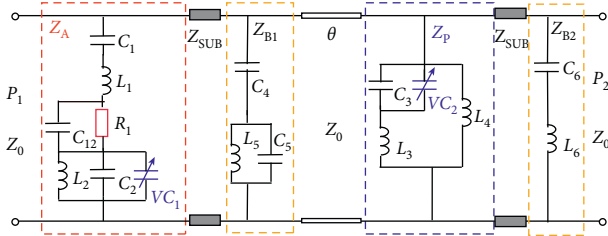


FIGURE 3: Equivalent circuit of the FSR.

Ansyz High Frequency Simulation Software (HFSS). Two results agree reasonably well with each other, especially at low frequencies, which means that the ECM is valid. At high frequencies, the mutual coupling between the FSS and the biasing network becomes stronger and more complex, which cannot be modelled with a simple circuit. Consequently, there is deviation between the two results. Figure 4(c) shows the absorptivity calculated with  $Abs. = 1 - |S_{11}|^2 - |S_{21}|^2$ , where  $S_{11}$  and  $S_{21}$  represent the reflection and transmission coefficients. Two absorptive bands, whose absorptivity is larger than 80% at 2.16–3.38 GHz and 4.38–7.24 GHz, are achieved. The dimensions for Figure 1 and the values for components in the ECM are given in Table 1. It should be mentioned that the presented structure has very low cross-polarization components, as shown in Figure 4(d), where  $S_{11}^{xx}$  and  $S_{21}^{xx}$  represent the reflection and transmission of copolarization, and  $S_{11}^{yx}$  and  $S_{21}^{yx}$  denote the reflection and transmission of cross-polarization. It means that the cross-polarization components hardly contribute to absorptivity.

Figure 5 shows the simulation results of the TFSR under the normal incidence. The passband is decreased from 4.78 to 3 GHz as the capacitances of  $VC_1$  is increased from 0 to 0.68 pF and  $VC_2$  from 0.05 to 0.6 pF. Table 2 provides the performances which include the bandwidth of passband, the maximum insertion loss (IL), and the lower and higher absorptive bands of  $|S_{11}| < -10$  dB.

The simulation results of the oblique incidence are shown in Figure 6. Both for the lower frequency at 3 GHz and for the high frequency at 4.72 GHz, the performances remain stable as the incident angle rose up to  $30^\circ$ .

### 3. Experiment Results and Discussion

To verify the design, a prototype was fabricated and measured. Considering the power of the full-wave simulator and the experimental cost, only parts of performances are measured. Figure 7(a) shows the prototype which is composed of  $7 \times 7$  unit cells within a total size of  $220 \text{ mm} \times 220 \text{ mm}$ . Between two FSSs, plastic nuts and screws are used to support the space of 12.5 mm. The free space measurement system consisting of one vector network analyzer (Keysight N5234A) and two antennas in an anechoic chamber is used to measure the reflection and transmission coefficients of the tunable FSR, as shown in Figure 7(b). The tunable range of the passband largely depends upon the capacitance tuning range of the used varactors. Varactors modelled SMV2019-079LF [26] are chosen to change the capacitance from 0.3 to 2.22 pF as their reverse bias voltage decreased from 20 to 0 V. For lower capacitance, MAVR-011020-1411 produced by MACOM is a choice [27].

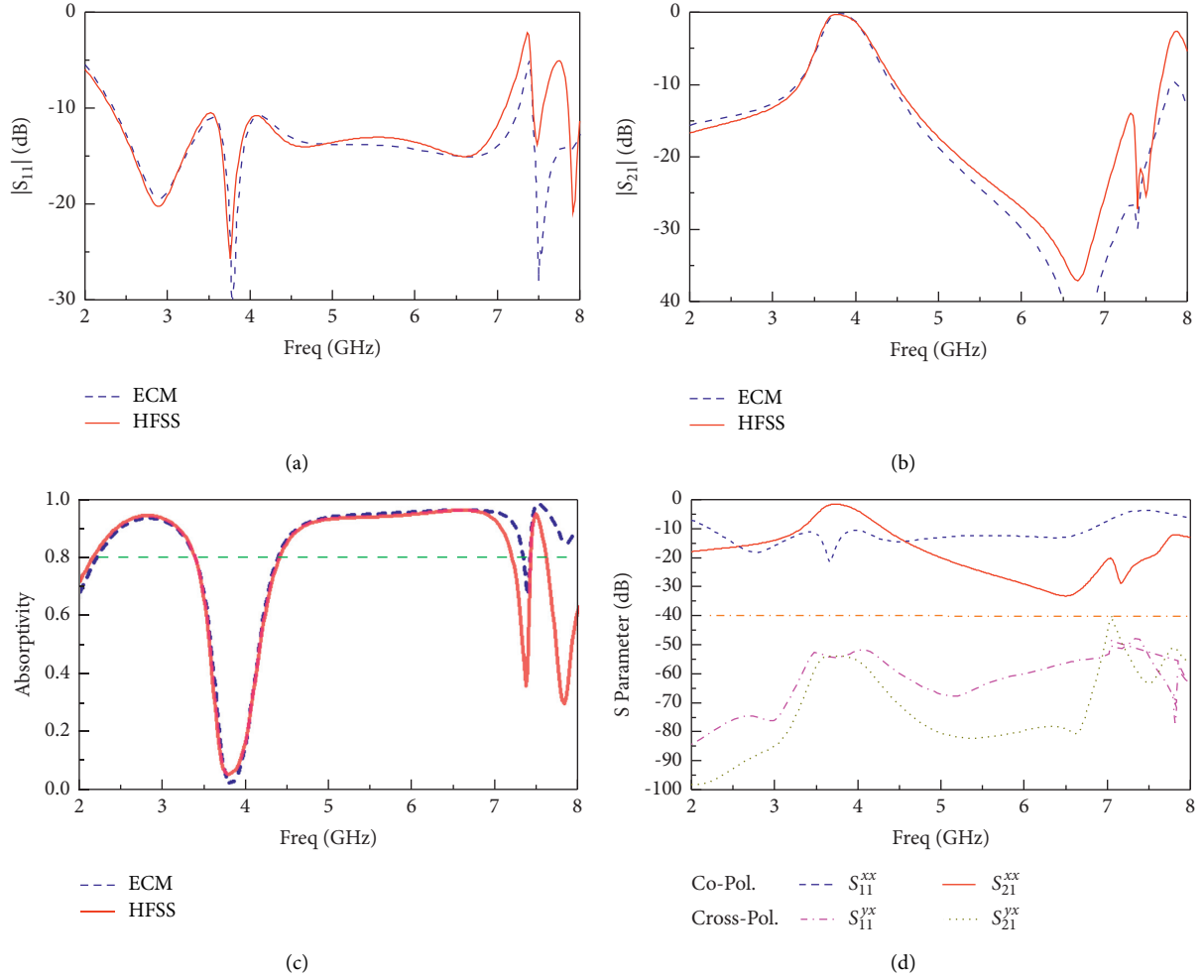


FIGURE 4: Results got from ECM and HFSS: (a) reflection, (b) transmission, (c) absorptivity, and (d) cross-polarization components.

TABLE 1: Dimensions for Figure 1 and values for components in the ECM.

Symbol	$l_1$	$l_2$	$l_3$	$l_4$	$l_5$	$l_6$	$l_7$	$l_8$	$l_9$
Value (mm)	17.3	12	3.3	4	3	9	1	1	1
Symbol	$w_1$	$w_2$	$w_3$	$w_4$	$g_1$	$r_1$	$r_2$	$h_1$	$h_2$
Value (mm)	4.0	6.0	0.5	0.5	05	9	8	0.5	12.5
Symbol	$L_1$	$L_2$	$L_3$	$L_4$	$L_5$	$L_6$		$Z_{SUB}$	$Z_0$
Value (nH)	12.466	3.462	0.548	1.857	1.581	2.645		254 $\Omega$	377 $\Omega$
Symbol	$C_1$	$C_2 + VC_1$	$C_3 + VC_2$	$C_4$	$C_5$	$C_6$	$C_{12}$	$R_1$	$R_b$
Value (pF)	0.137	0.328	0.388	0.017	0.288	0.119	0.001	400 $\Omega$	10 k $\Omega$

Figure 8 shows the measured  $|S_{11}|$ ,  $|S_{21}|$ , and absorptivity under the normal incidence. Three different bias voltages of 5, 7, and 19 V for  $VC_1$  and 4, 6 and 18 V for  $VC_2$ , respectively, are plotted. As the reversed voltage increased, the passband increases from 2.6 to 3.77 GHz. The measured insertion losses shown in Figure 8 are larger than the simulated results shown in Figure 5, especially at the low frequencies. High insertion loss results in large absorptivity at the passband, as shown in Figure 8(c). The main reason is that the series resistance ( $R_s$ ) of varactors is voltage dependent, and it is higher at low reversed bias voltage [28, 29]. Figure 9(a) shows the comparison of the simulated

insertion losses of different series resistances. The IL is increased from 0.32 to 2.5 dB as  $R_s$  is increased from 0 to 10  $\Omega$ . A typical equivalent circuit for a varactor is also shown in the figure, where  $L_s$  is the parasitic inductance associated with the package and bonding wires of the diode,  $C_p$  is the package capacitance, and  $C_j$  is the varactor junction capacitance. The second reason is the truncation of the structure, namely, only a finite array of  $2\lambda \times 2\lambda$  at 3 GHz has been fabricated and measured, but an infinite periodic array was simulated.

Figures 9(b) and 9(c) show the comparison of the simulation results of  $VC_1 = 0.3$  pF,  $VC_2 = 0.28$  pF, and

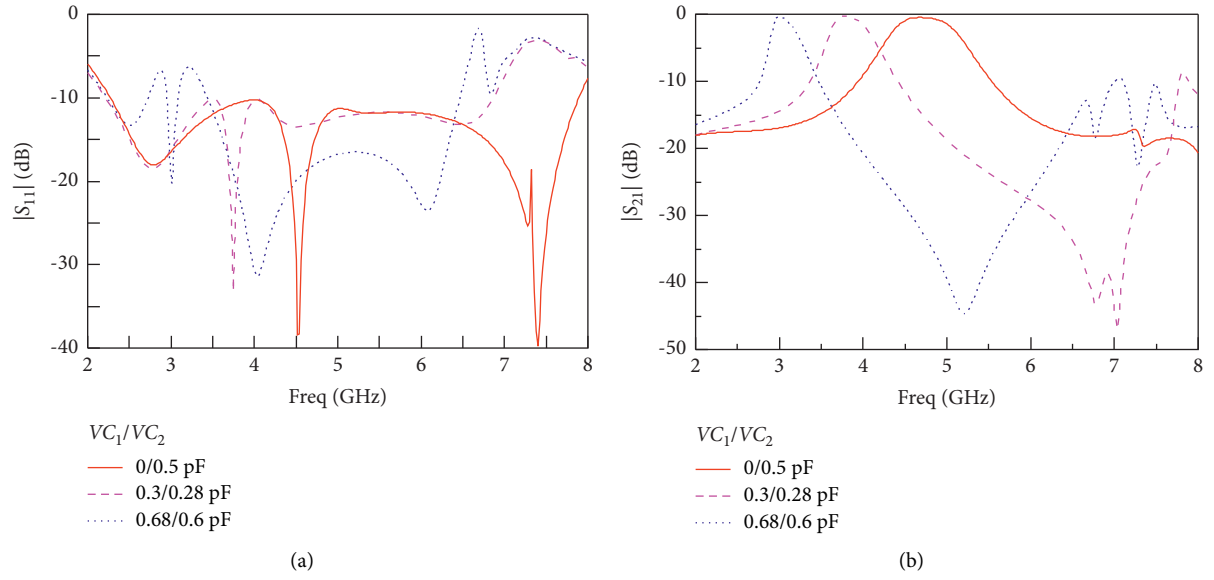
FIGURE 5: The simulated S parameter of the tunable passband: (a)  $|S_{11}|$  and (b)  $|S_{21}|$ .

TABLE 2: Performance of the tunable FSR.

$VC_1$ (pF)	0	0.3	0.68
$VC_2$ (pF)	0.05	0.28	0.6
Passband_3 dB (GHz)	4.33–5.13	3.62–4.14	2.91–3.21
Insertion loss (dB)	0.52	0.32	0.3
Lower abs. band (GHz)	2.22–3.94	2.20–3.37	2.18–2.76
Higher abs. band (GHz)	5.54–7.96	4.48–6.94	3.46–6.41

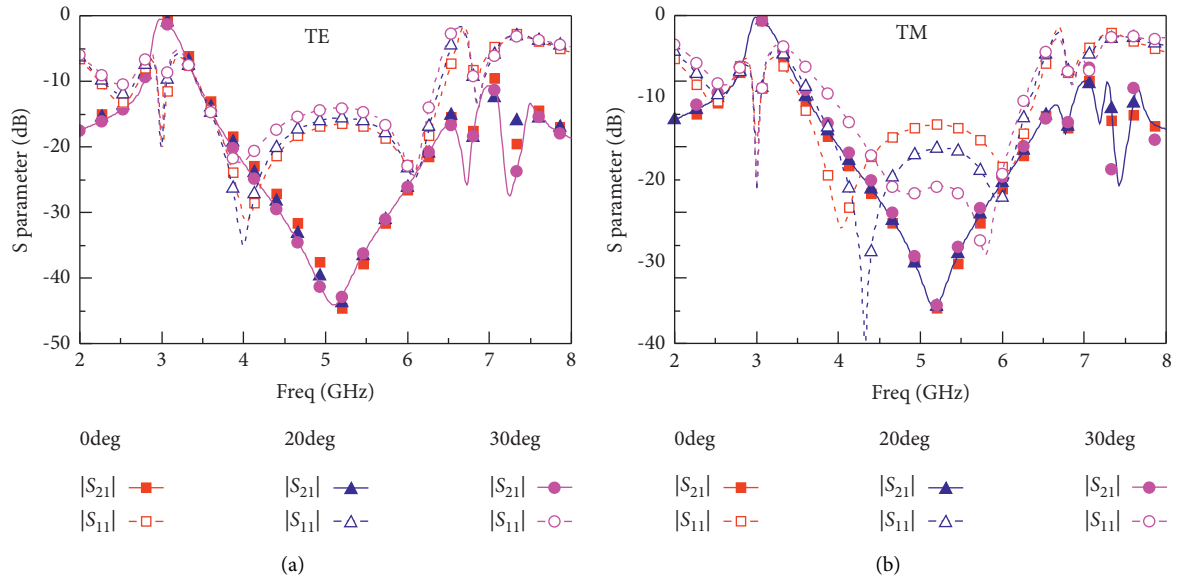


FIGURE 6: Continued.



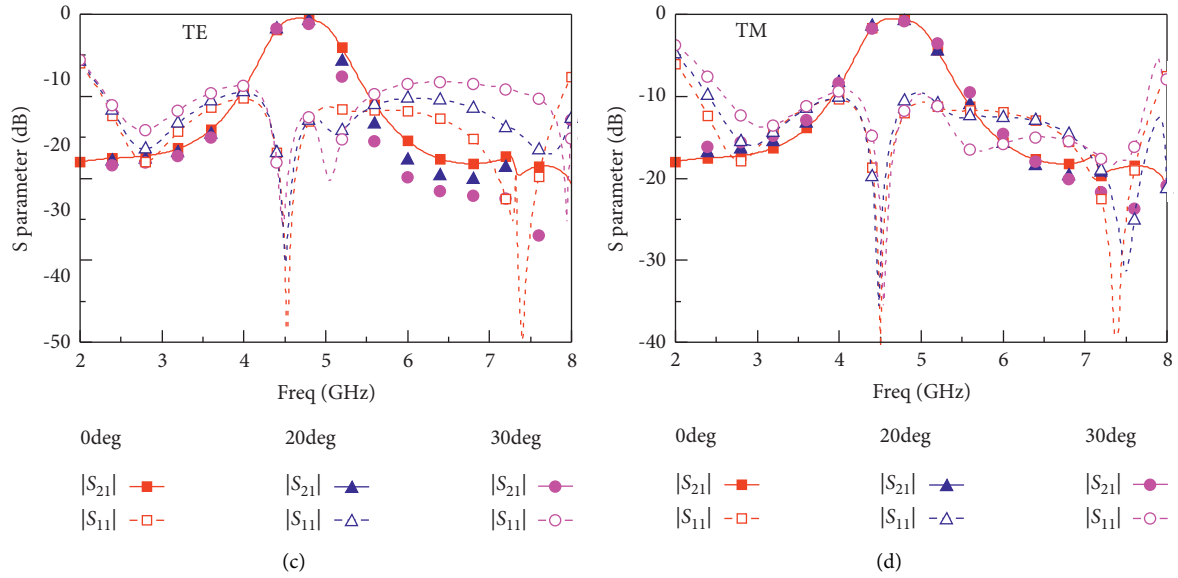


FIGURE 6: The simulation results under the oblique incidence: (a) TE at 3 GHz, (b) TM at 3 GHz, (c) TE at 4.72 GHz, and (d) TM at 4.72 GHz.

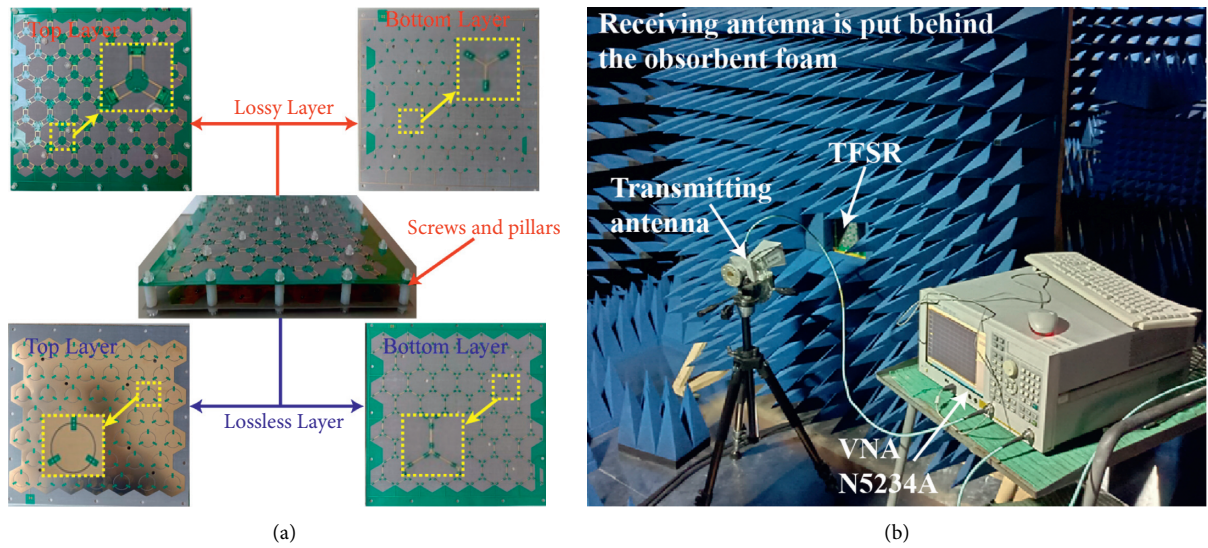


FIGURE 7: Prototype and measurement system. (a) Photo of the TFSR and (b) measurement system.

experiment results of the bias voltage of 18 and 20 V. The measured band of  $|S_{21}| \geq -3$  dB covers from 3.50 to 4.09 GHz and the band of  $|S_{11}| \leq -10$  dB covers from 2.2 to 7.86 GHz. Almost same minimum insertion loss of 1.5 dB is obtained for two results at 3.77 GHz, owing to the consideration of the series resistance of varactors. Some discrepancies exist between the two results, particularly at high frequency. Besides

the aforementioned reasons, another might be because some distribution parameters such as the package and soldered dot of the varactor diodes were not taken into account during the simulations.

Table 3 provides the comparison of the performances of the presented TFSR and some published designs with continuously tunable passband. For the bandwidth of

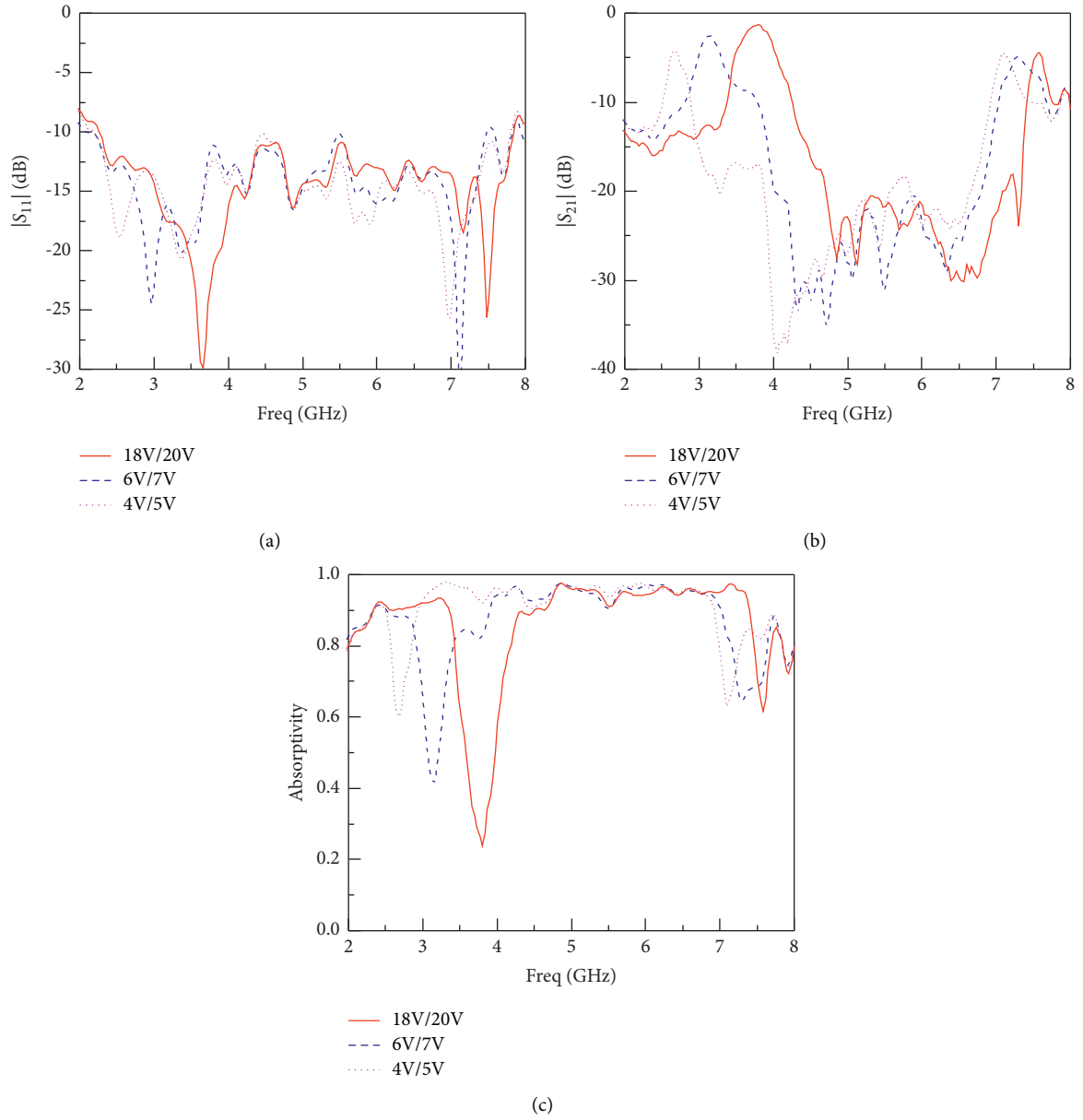


FIGURE 8: Measured results of the presented TFSR with different bias voltage under the normal incidence. (a)  $|S_{11}|$ . (b)  $|S_{21}|$ . (c) Absorptivity.

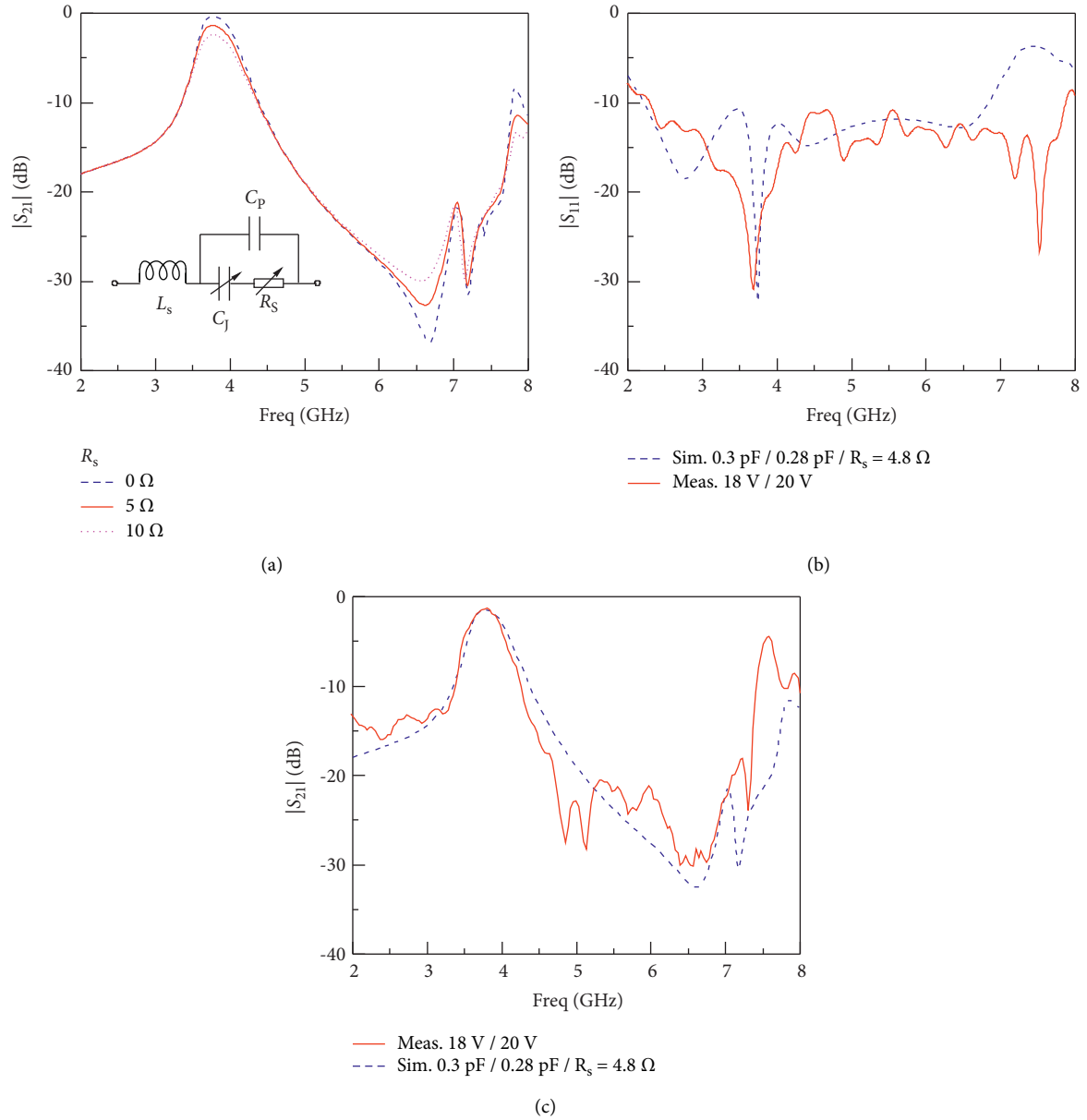


FIGURE 9: Comparisons of the simulated and measured S-parameters. (a) Effect of series resistance on insertion loss, (b)  $|S_{11}|$ , and (c)  $|S_{21}|$ .

TABLE 3: Comparisons between this work and some published results.

Ref	Simulation			Measurement			Thickness ( $\lambda_L$ )	Pol.
	Cap. (pF)	Tunable (GHz)	Voltage (V)	Tunable (GHz)	IL (dB)	$BW_{S_{11}}$ (GHz)		
[12]	0.12–0.52	2.7–3.4	0–22	1.6–3.3	3.4–9.3	1.9–5.4	0.092	Dual
[13]	0.12–0.38	3.8–5.2	4–16	3.8–5.2	0.59–2.5	2.4–6.58	0.107	Single
[14]	0.15–0.5	3.33–5.13	4–18	2.8–4.2	1.7–6.5	2.67–7.89	0.134	Dual
This work	0–0.68	3.0–4.78	5–20	2.6–3.77	1.5–5	2.2–7.86	0.099	Dual

$|S_{11}| \leq -10$  dB ( $BW_{S_{11}}$ ), this work is wider than the others. The minimum insertion loss of this work is lower than [12, 14]. The thickness of the design, corresponding to the longest absorptive wavelength ( $\lambda_L$ ), is slightly thicker than [12] but thinner than [13, 14].

#### 4. Conclusion

A tunable frequency-selective rasorber has been successfully designed, and some performances have been measured for verification. The tunability is achieved by integrating the



varactors and biasing network on both the absorptive FSS realized with tripole elements and the bandpass FSS realized with slot ring elements. Measured results show that designed TFSR has a continuous tuning range from 2.6 to 3.77 GHz for the center transmission frequency as the reverse biasing voltage of the varactors are decreased from 20 to 5 V. The proposed TFSR has potential applications in reconfigurable stealthy antenna-radome systems owing to the tunable transmission band in wide absorptive bands.

## Data Availability

The data used to support the findings of this study are included within the article.

## Conflicts of Interest

The authors declare that they have no conflicts of interest.

## Acknowledgments

This work was supported by the National Natural Science Foundations of China under grant No. 62071435.

## References

- [1] A. A. Omar, H. Huang, and Z. Shen, "Absorptive frequency-selective reflection/transmission structures: a review and future perspectives," *IEEE Antennas and Propagation Magazine*, vol. 62, no. 4, pp. 62–74, 2020.
- [2] W. S. Arceneaux, R. D. Akins, and W. B. May, "Absorptive/transmissive radome," U.S. Patent 5 400 043, 1995.
- [3] B. A. Munk, *Metamaterials: Critique and Alternatives*, Wiley, Hoboken, NJ, USA, 2009.
- [4] Z. Wang, Q. Zeng, J. Fu et al., "A high-transmittance frequency-selective rasorber based on dipole arrays," *IEEE Access*, vol. 6, pp. 31367–31374, 2018.
- [5] S. Yu, N. Kou, Z. Ding, and Z. Zhang, "Harmonic-suppressed frequency selective rasorber using resistive-film sheet and square-loops resonator," *IEEE Antennas and Wireless Propagation Letters*, vol. 19, no. 2, pp. 292–296, 2020.
- [6] Q. Guo, J. Su, Z. Li, L. Y. Yang, and J. Song, "Absorptive/transmissive frequency selective surface with wide absorption band," *IEEE Access*, vol. 7, pp. 92314–92321, 2019.
- [7] Q. Guo, Z. Li, J. Su, L. Y. Yang, and J. Song, "Dual-polarization absorptive/transmissive frequency selective surface based on tripole elements," *IEEE Antennas and Wireless Propagation Letters*, vol. 18, no. 5, pp. 961–965, May 2019.
- [8] X. Zhang, W. Wu, L. Huang, Y. Ma, and N. Yuan, "Design of dual-absorptive-bands frequency selective rasorber with minkowski loop arrays," *IEEE Antennas and Wireless Propagation Letters*, vol. 18, no. 9, pp. 1843–1847, 2019.
- [9] Y. Wang, S.-S. Qi, Z. Shen, and W. Wu, "Ultrathin 3-D frequency selective rasorber with wide absorption bands," *IEEE Transactions on Antennas and Propagation*, vol. 68, no. 6, pp. 4697–4705, 2020.
- [10] T. Deng, Y. Yu, Z. Shen, and Z. N. Chen, "Design of 3-D multilayer ferrite-loaded frequency-selective rasorbers with wide absorption bands," *IEEE Transactions on Microwave Theory and Techniques*, vol. 67, no. 1, pp. 108–117, 2019.
- [11] Y. Zhang, B. Li, L. Zhu, Y. Tang, Y. Chang, and Y. Bo, "Frequency selective rasorber with low insertion loss and dual-band absorptions using planar slotline structures," *IEEE Antennas and Wireless Propagation Letters*, vol. 17, no. 4, pp. 633–636, 2018.
- [12] L. Wu, S. Zhong, J. Huang, and T. Liu, "Broadband frequency-selective rasorber with varactor-tunable interabsorption band transmission window," *IEEE Transactions on Antennas and Propagation*, vol. 67, no. 9, pp. 6039–6050, 2019.
- [13] Y. Wang, S.-S. Qi, Z. Shen, and W. Wu, "Tunable frequency-selective rasorber based on varactor-embedded square-loop array," *IEEE Access*, vol. 7, pp. 115552–115559, 2019.
- [14] Q. Guo, Z. Zhao, J. Su, and Z. Li, "Dual-polarization absorptive/transmissive frequency-selective surface with tunable passband," *IEEE Transactions on Electromagnetic Compatibility*, vol. 63, no. 5, pp. 1347–1356, 2021.
- [15] J. Tian, B. Chen, B. Jiang, R. Li, S. Lei, and H. Hu, "Reconfigurable frequency selective rasorber covering extremely wide transmission frequency range," *IEEE Access*, vol. 8, pp. 225566–225580, 2020.
- [16] S. C. Bakshi, D. Mitra, and F. L. Teixeira, "FSS-based fully reconfigurable rasorber with enhanced absorption bandwidth and simplified bias network," *IEEE Transactions on Antennas and Propagation*, vol. 68, no. 11, pp. 7370–7381, 2020.
- [17] S. C. Bakshi, D. Mitra, and S. Ghosh, "A frequency selective surface based reconfigurable rasorber with switchable transmission/reflection band," *IEEE Antennas and Wireless Propagation Letters*, vol. 18, no. 1, pp. 29–33, 2019.
- [18] X. Yan, X. Kong, Q. Wang et al., "Water-based reconfigurable frequency selective rasorber with thermally tunable absorption band," *IEEE Transactions on Antennas and Propagation*, vol. 68, no. 8, pp. 6162–6171, 2020.
- [19] S. C. Bakshi, D. Mitra, and F. L. Teixeira, "Wide-angle broadband rasorber for switchable and conformal application," *IEEE Transactions on Microwave Theory and Techniques*, vol. 69, no. 2, pp. 1205–1216, 2021.
- [20] Z. Zhu, Y. Li, J. Zhang et al., "Absorptive frequency selective surface with two alternately switchable transmission/reflection bands," *Optics Express*, vol. 29, no. 3, pp. 4219–4229, 2021.
- [21] A. de Lustrac, B. Ratni, G.-P. Piau, Y. Duval, and S. N. Burokur, "Tri-state metasurface-based electromagnetic screen with switchable reflection, transmission, and absorption functionalities," *ACS Applied Electronic Materials*, vol. 3, no. 3, pp. 1184–1190, 2021.
- [22] H. Li, H. Yuan, F. Costa, Q. Cao, W. Wu, and A. Monorchio, "Improved dual-polarized wideband multifunctional switchable absorber/reflector based on active frequency selective surfaces," *Optics Express*, vol. 29, no. 20, pp. 31036–31047, 2021.
- [23] F. Costa, A. Monorchio, and G. Manara, "Efficient analysis of frequency-selective surfaces by a simple equivalent-circuit model," *IEEE Antennas and Propagation Magazine*, vol. 54, no. 4, pp. 35–48, 2012.
- [24] A. Tretyakov, *Analytical Modeling in Applied Electromagnetics*, Artech House, Norwood, MA, USA, 2003.
- [25] R. J. Langley and E. A. Parker, "Equivalent circuit model for arrays of square loops," *Electronics Letters*, vol. 18, no. 7, pp. 294–296, 1982.
- [26] Skyworks Solutions, Inc., "Skywork data sheet," 2019, <https://www.skyworksinc.com/en/Products/Diodes/SMV2019-Series>.
- [27] MACOM Technology Solutions Inc., [Online]. Available: <https://www.macom.com/products/product-detail/MAVR-011020-1411>.
- [28] T. P. Lee, "Evaluation of voltage dependent series resistance of epitaxial varactor diodes at microwave frequencies," *IEEE Transactions on Electron Devices*, vol. 12, no. 8, pp. 457–470, 1965.
- [29] P. Phillippe, W. El-Kamali, and V. Pauker, "Physical equivalent circuit model for planar Schottky varactor diode," *IEEE Transactions on Microwave Theory and Techniques*, vol. 36, no. 2, pp. 250–255, 1988.